Journal of
Polymer Materials

Tech Science Press

https://doi.org/10.32604/jpm.2026.078127

ARTICLE

Quasi 2D Silicon Nanosheet and Polyaniline Nanocomposites: Structural and Photoluminescence Properties

Debosmita Karar[1,*], Ashit Kumar Pramanick[2] and Mallar Ray[3]

[1]Biomaterials and Medical Devices Division, CSIR-Central Glass and Ceramic Research Institute, Jadavpur, Kolkata, India
[2]Materials Science and Technology Division, CSIR-National Metallurgical Laboratory, Jamshedpur, Jharkhand, India
[3]School of Engineering and Sciences, Tecnológico de Monterrey, Av. Eugenio Garza Sada 2501 Sur, Tecnológico, Monterrey, Nuevo León, Mexico

*Corresponding Author: Debosmita Karar. Email: karardebosmita@gmail.com

Received: 24 December 2025; Accepted: 24 March 2026; Published: 30 June 2026

ABSTRACT: Experimental preparation of graphene like 2D silicon is a great challenge due to the dominant sp^3 hybridization in silicon. We have synthesized quasi 2D crystalline silicon nanosheets by topochemical exfoliation of layered Zintl phases, which bear signatures of properties predicted theoretically. Quasi-two-dimensional silicon nanosheets were uniformly dispersed within a conducting polyaniline matrix to fabricate solid-state nanocomposites with varying silicon loadings. The resulting polyaniline–quasi-2D silicon composites were systematically examined for their structural characteristics and optical emission behavior. Notably, the nanocomposites exhibit intense photoluminescence at room temperature, with an emission efficiency significantly higher than that of pristine quasi-2D silicon. The functional characteristics of the nanocomposite can be tailored by adjusting the loading and spatial dispersion of the nanoscale components, the nature of the host matrix, and the interfacial interactions between them. This nanocomposite is a promising candidate for the development of efficient thermoelectric material and has huge potential for applications in electronics and sensing.

KEYWORDS: 2D material; silicon nanosheet; polyaniline; photoluminescence

1 Introduction

Among the various silicon nanostructures, two-dimensional silicon has received comparatively limited attention, primarily because of the experimental challenges involved in synthesizing stable, atomically thin silicon layers. In 1994, Takeda and Shiraishi first demonstrated the possibility of the existence of a 2D Si network [1], and investigated the structure of a hypothetical infinite 2D network using the first principle local density functional method [2,3]. The advent of graphene ushered in a renewed worldwide interest in 2D materials and subsequently a variety of exact and quasi 2D materials were prepared and investigated [4–8]. However, experimental realization of exact 2D Si remained elusive. This is because structurally a 2D allotrope of Si is energetically not favored. Si atoms tend to adopt sp^3 hybridization over sp^2. Attempts have been made to prepare quasi 2D Si sheets by exfoliating layered silicide materials [9,10], and by epitaxial growth of Si layers on different substrates [11,12]. Chemical exfoliation of Zintl phases of Si has resulted in the formation of quasi 2D Si sheets that are usually surface-terminated by functional groups composed of oxygen, hydrogen, and hydroxyl radicals [9,10]. In contrast, efforts to grow silicon monolayers epitaxially on metal substrates have achieved only limited success, and isolating the intrinsic properties of the two-dimensional silicon network from substrate-induced effects remains a significant challenge [13,14].

In the absence of silicene—the ideal monolayer of Si atoms, quasi 2D nanosheets of Si present an interesting alternative as they exhibit various features such as room temperature photoluminescence (PL) and remarkable Hall mobility [15]. However, the chemically exfoliated Si nanosheets require a substrate or some background matrix in which they need to be dispersed in order to exploit their unique properties. A solid-state nanocomposite formed by dispersing the 2D sheets also offers tunability in various properties that could be achieved simply by varying the concentration and distribution of the nanoscale building blocks, the host matrix, and the interactions between them [16]. In principle, the electrical and thermal conductivities in such systems can be independently varied, thereby rendering them amenable to the development of high efficiency thermoelectric materials [17,18]. In this regard, polyaniline (PANI), a π-conjugated, conducting polymer, offers an excellent choice as a background matrix due to its simple and inexpensive synthesis procedure, flexibility and mechanical strength, appropriate redox and anion exchange properties, and good environmental stability [19,20]. Most importantly, the electrical conductivity of PANI can be tuned over a very wide range ($<10^{-12}$ to 10^{5} S cm^{-1}) from nearly insulating to metal-like by controlled doping [21]. Besides being a promising candidate for efficient thermoelectricity, a nanocomposite of quasi 2D Si in PANI matrix, also holds considerable potential for flexible electronics and sensing.

Due to the tunable electrical properties and flexibility of PANI, it has been widely used as a matrix for dispersing a variety of nanostructures [22]. Among many others, different types of semiconductor quantum dots [23,24], carbon nanotubes [25,26], reduced graphene oxide (rGO), carbon dots and graphene quantum dots [27–29] have been extensively used as nanofillers in PANI matrix in attempts to derive novel and/or multifunctional properties. The interaction between PANI and these nanostructures has been exploited for applications in efficient energy storage and harvesting, catalysis, sensing, etc. However, despite such huge advances in 2D carbon and PANI composites, there is no published literature on composites based on 2D Si and PANI.

This work reports the preparation of quasi-2D systems of Si by chemical exfoliation of the layered Zintl phase of Si and subsequently incorporates the 2D Si flakes in a PANI matrix. The Si 2D nanosheet incorporated PANI exhibit intense room temperature PL. We have investigated the detailed structural features and the optical emission properties of this remarkable nanocomposite material. To the best of our knowledge, this is the first report on a Si nanosheet decorated PANI composite.

2 Materials and Methods

2.1 Preparation of Quasi 2D Si Nanosheets

Quasi 2D Si nanosheets were prepared via a topochemically driven exfoliation process starting from a layered material calcium silicide ($CaSi_2$) powder following the route described by Nakano et al. Briefly, ~1g $CaSi_2$ (Sigma Aldrich) was subjected to constant stirring for 72 h in 1L of 35% HCl to transform the silicide into siloxene at ~0°C–4°C. The resulting suspension was filtered and rinsed with ethanol, yielding a greenish-yellow solid identified as $Si_6H_3(OH)_3$, which precipitated from the initially translucent colloidal solution.

2.2 Preparation of PANI

PANI was synthesized by chemical oxidative polymerization of aniline (Merck). The aniline monomer was distilled with an excess of zinc dust until the liquid turned colorless. A solution of 40 mM of camphor sulphonic acid (CSA) (Sigma Aldrich) and 3 mM of cetyltrimethylammonium bromide (CTAB) (Sigma Aldrich) was stirred for 1 h and subsequently, 4 mL of neat aniline was added into the solution. The reaction mixture was kept at approximately 0°C–5°C using an ice bath and subjected to magnetic stirring at about 500 rpm for 1 h. 21.4 mM of ammonium persulfate (APS) (Sigma Aldrich), an oxidant, was added dropwise

into the previous solution containing PANI. The quantities of the different reactants ensured fixed molar ratios of 1:2 and 1:1 between aniline and CSA and between aniline and APS, respectively. The mixture was stirred at the same rate and the temperature was maintained around 0°C–5°C for 24 h. Filtration was followed by extensive rinsing with 4 L of DI water, followed by several ethanol washes and again with 1 L of DI water. Subsequently, the PANI precipitate was collected and dried at a temperature of 50°C in a vacuum oven for 12 h and the resulting blackish green powder was stored and used for characterization.

2.3 Preparation of the Nanocomposite

The nanocomposite preparation is similar to the procedure of preparation of PANI. Before adding the aniline monomers, the as-synthesized 2D nanosheets of Si were added to the solution containing CTAB and CSA. Five different composite samples were prepared by introducing 0.2, 0.4, 0.6, 1.0 and 1.6 gm of Si nanosheets in 4 mL of aniline, which respectively correspond to 5, 10, 15, 25 and 40 weight%, of quasi 2D Si with respect to aniline. Subsequently the samples were separated by filtration, thoroughly washed, and subsequently vacuum-dried at 50°C for 12 h. The nanocomposites corresponding to 5%, 10%, 15%, 25% and 40%, of 2D nanosheets were named as P5, P10, P15, P25 and P40, respectively (Fig. 1).

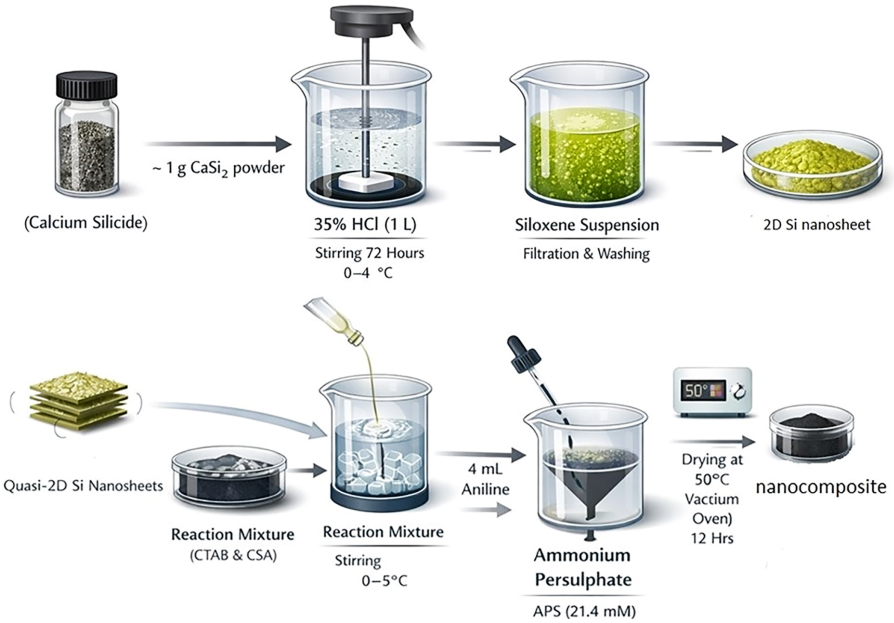

Figure 1: Schematic of the synthesis.

Investigation of the crystalline property of the synthesized powder of the composites was carried out by using a Brucker D8 advanced diffractometer operating at 40 kV, using Cu Kα1 (λ = 1.54 Å) radiation. Data were recorded for 2θ varying from 10° to 70° with a step size of 0.02° per second. HR-TEM investigations were carried out to characterize the synthesized composites with PANI. A JEOL, JEM-2200 FS, analytical electron microscope, equipped with a 200 kV field emission gun was used for all HR-TEM imaging. FT-IR absorption spectra of the samples were recorded by a JASCO 4700 LE FTIR spectrometer. Both transmission and ATR mode recordings were performed. A double beam JASCO V-750 UV-visible spectrometer was employed in this study to record the absorption spectra of the colloidal samples. Measurement of PL was carried out using Horiba Jobin Yvon, Flurolog-3 (Nanolog) spectrofluorometer (model FL3-22) equipped with a 450 W xenon lamp. Absolute PL quantum yield (QY) was determined by using an integrating sphere.

3 Results and Discussion

The XRD patterns of the different samples—blank PANI, as-prepared quasi 2D nanosheets of Si and the nanocomposites containing different wt% of 2D Si in PANI (P5, P10, P15, P25 and P40) are presented in Fig. 2. The XRD profile of blank PANI, shown in Fig. 2a demonstrates the typical features of PANI in its emeraldine salt conformation which is composed of two broad humps peaking at $2\theta \approx 15.4°$ and 19.8° and a relatively sharper peak at $2\theta \approx 25.4°$. These three features correspond to the Bragg reflections from (010), (100) and (110) planes of pure PANI, respectively [30]. The broad diffraction features observed for PANI are attributed to the repeating units of the polymer chains and to the structural periodicity along directions perpendicular and parallel to the polymer backbone [31]. Consistent with the behavior of highly doped emeraldine salt, the comparatively sharper reflection at 25.4° exhibits greater intensity than the two broader features [30]. The XRD profile of the as-synthesized Si nanosheets obtained by chemical exfoliation of $CaSi_2$, shown in Fig. 2b, demonstrates peaks due to (111), (220) and (311) planes of crystalline Si. The XRD patterns of all the composites shown in Fig. 2c are primarily governed by the crystalline signatures of silicon present in the sample and the PANI characteristics are almost completely masked, except for a weak signature of the (110) planes. This signature evidently becomes weak as Si content increases in the nanocomposite samples. Comparing the XRD patterns of blank PANI and quasi 2D Si samples we see that the gross individual crystalline features of both the ingredients—Si nanosheets and PANI, remain unaltered in the nanocomposites.

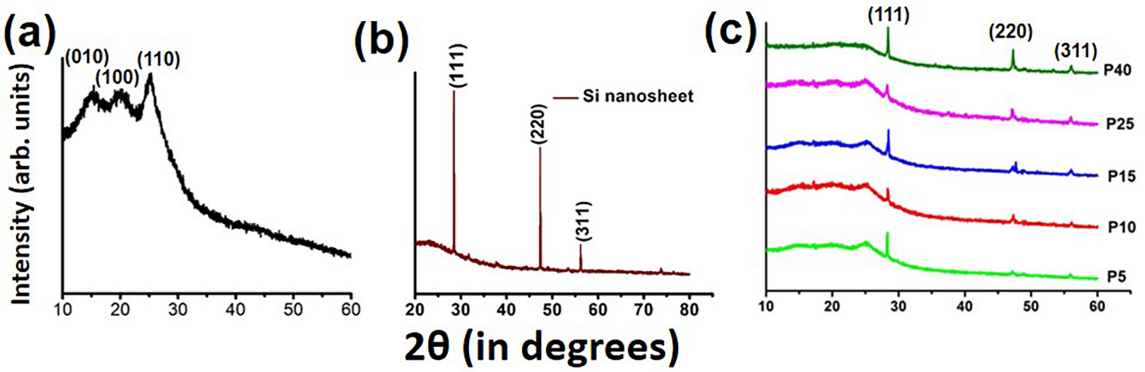

Figure 2: XRD profiles of the nanocomposites. (**a**) The XRD of blank PANI revealing the features of the sample; (**b**) XRD of as-prepared quasi 2D Si sheets; and (**c**) XRD profiles of the different nanocomposite samples (P5, P10, P15, P25, P40).

The HRTEM images of blank PANI are shown in Fig. 3a–c. From Fig. 3a–c, it is evident that the sample comprises a combination of quasi-one-dimensional nanotube-like structures and quasi-two-dimensional nanosheet-like structures. The selected area electron diffraction pattern (SAEDP) corresponding to the bright field image in Fig. 3a is shown as an inset. The diffraction rings due to the (110) plane of crystalline PANI can be easily identified and are marked in the figure. The nanotube-like feature of the 1D PANI is also clear from the micrograph shown in Fig. 3b, wherein we can clearly identify an annular structure that is a signature of nanotubes. Magnified image of each individual 1D PANI reveals a similar kind of morphology. The crystalline nature of the one-dimensional PANI nanotubes is clearly visible in the inset of Fig. 3b, where we can see fringes corresponding to the (110) plane of PANI. Electron diffraction on areas selected to have the 2D structure only gives us a featureless pattern that is typical of an amorphous sample as shown in Fig. 3c. The HRTEM, therefore, builds upon the findings of XRD and establishes that the PANI sample is semi-crystalline and consists of an entangled network of crystalline quasi 1D and largely amorphous quasi 2D structures.

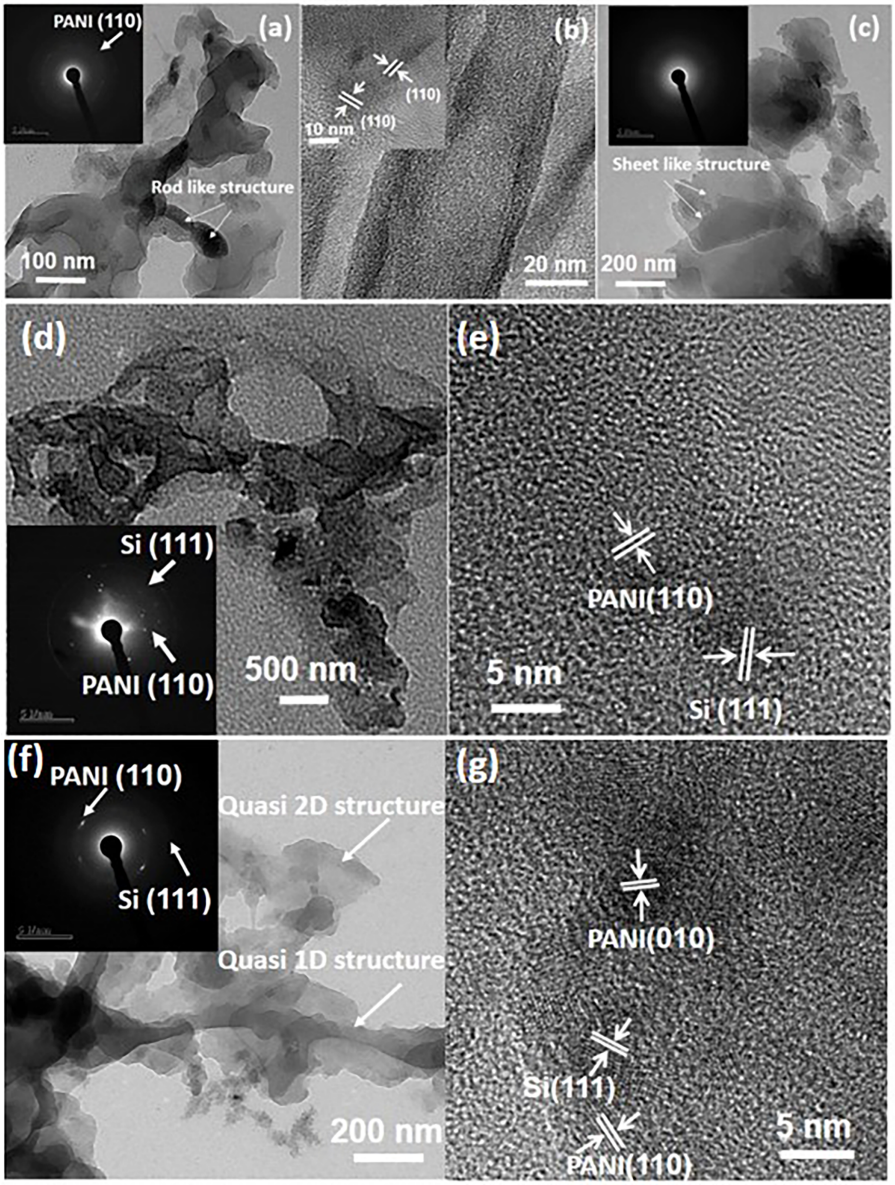

Figure 3: HRTEM of PANI and the composites at different magnifications. (**a**) Bright field image showing that the overall structure and morphology of PANI consists of a mixed network of quasi 1D and quasi 2D structures. Inset shows the SAEDP corresponding to the bright field image. (**b**) An image showing a single 1D PANI having an annular structure suggesting the formation of nanotubes. Inset shows the crystalline fringes. (**c**) Bright field image showing sheet-like structure of PANI, inset shows the corresponding featureless SAEDP. (**d**) Bright field images of sample P5 showing arbitrarily shaped networks of PANI and Si nanosheets, the inset shows the SAEDP corresponding to (**d**). (**e**) High magnification image revealing the crystalline fringes of Si and PANI. (**f**) Bright field image of P40 showing arbitrarily shaped networks of PANI and Si nanosheets, the inset shows the SAEDP corresponding to the image. (**g**) High magnification image revealing the crystalline fringes of Si and PANI.

HRTEM micrographs of the nanocomposites—the one with the least concentration of 2D Si nanosheets in PANI (sample P5) and the one with maximum concentration of Si in PANI (sample P40), are shown in Fig. 3d–g. The HRTEM micrograph of P5 shown in Fig. 3d reveals agglomerated lump-like structures. A closer inspection reveals that these lump-like structures are mesh-like networks of quasi 1D and quasi 2D

structures. The SAEDP shown as an inset of Fig. 3d demonstrates the presence of crystalline nanostructures of both Si and PANI since we find distinct rings corresponding to the (110) plane of PANI and (111) plane of Si. Crystalline fringes of the (111) plane of Si and the (110) plane of PANI, are identified and marked in the high magnification images shown in Fig. 3e. Overall, the HRTEM images of the P5 composite samples reveal the formation of a nanocomposite of PANI and dispersed quasi 2D Si structures. The HRTEM images of the sample containing the maximum amount of quasi 2D Si (sample P40) in the PANI matrix are shown in Fig. 3f,g. The gross features of the micrographs corresponding to P40 are similar to those of the sample P5. We see a disordered network of entangled quasi 1D and quasi 2D structures. The crystalline character of Si and PANI is revealed from the SAEDP shown as an inset of Fig. 3f and the fringes observed in Fig. 3g. The relative abundance of Si as compared to sample P5 is also evident from the dominant Si features.

To investigate the chemical groups present in the samples, standard FTIR absorption studies were done. Fig. 4 represents the FTIR analysis of the composite samples along with blank PANI. In case of blank PANI (PB) the band observed at 695 cm^{-1} corresponds to the ring out-of-plane deformation of the monosubstituted phenylene ring. The band observed at 787 cm^{-1} corresponds to the C–H out-of-plane bending vibration [32]. The peaks in between 1010–1110 cm^{-1} are due to aromatic C–H in plane bending modes [33]. As our PANI sample exists in emeraldine salt form, positively charged nitrogen exists, and the peaks at 1230 and 1285 cm^{-1} indicate stretching of CN^{+} and stretching of aromatic C–N bonds, respectively [34]. The characteristic peaks at 1480 and 1563 cm^{-1} can be assigned to C–C stretching vibrations of the quinoid and benzenoid rings, respectively, which confirms the presence of emeraldine form. A weak band is observed at 1722 cm^{-1}, which can be assigned to the quinoid-imine stretching mode [35]. The peak at 2973 cm^{-1} corresponds to CH_3 symmetric stretching, while the band at 3200 cm^{-1} is attributed to N–H stretching [36]. All the signatures in PB sample confirm the formation of PANI in its conducting emeraldine salt form.

The positions of 1725, 2973 and 3200 cm^{-1} are almost the same for all the composite samples. With the decrease in Si percentage, i.e., from P40 to P5 samples, the peak at 695 cm^{-1} is observed with lower intensity in comparison to the PB sample. The peak at 787 cm^{-1} is observed with a lower wavenumber and the aromatic C–H in plane bending modes are concentrated only between 1030–1056 cm^{-1} with an increase in the Si percent. Interaction with silicon influences the electron density of the benzene ring, leading to a reduction in the stretching frequency of the aromatic C–H bonds. The intensity of 1230 cm^{-1} increases and at 1285 cm^{-1} the intensity decreases with an increase in the amount of Si and the peak at 1580 cm^{-1} becomes more prominent. The shoulder at 2290 cm^{-1} is present in all the composite samples and this arises from the Si–H stretching mode in O_3SiH [37]. There is a peak at 510 cm^{-1} present in all the samples except bare PANI. This is the signature Si-Si bond due to the presence of the Si-Si network [38].

Fig. 5 shows the variation of the absorption profile measured over a period of six months. The absorption profile undergoes a significant change during the first month following which the change slows down with time. We note the following features for the time variation of UV absorption: (i) the absorption peak at ~280 nm become broad and tends to merge with the broad absorption at higher wavelengths, (ii) the absorption in the near-UV range increases over time, which tends to mask the dominant sharp transition in UV region, and (iii) the entire absorption spectrum exhibits a continuous red-shift. These observations can be understood in terms of time dependent slow oxidation of low-dimensional Si that has been widely reported in literature [39]. Slow ambient oxidation leads to the formation of sub bandgap states inside the widened bandgap of quasi 2D Si. Hence, with time, the Si nanocrystal absorption is dominated by absorption of these sub bandgap states which progressively intrude inside the visible spectrum. Such continuous oxidation in Si NCs has been previously observed in various forms of nanocrystalline Si [40].

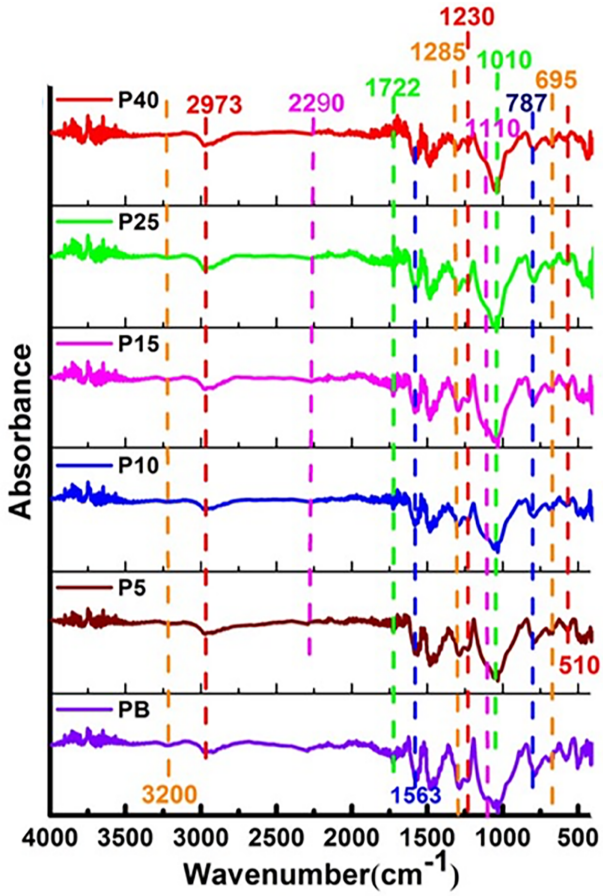

Figure 4: FTIR spectra of blank PANI and the nanocomposite samples.

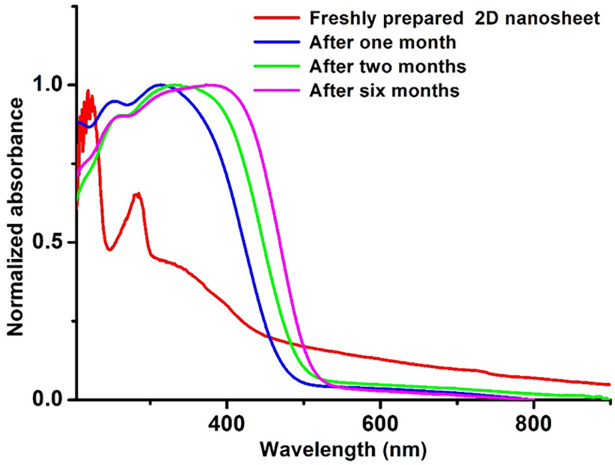

Figure 5: UV-visible absorption spectrum of Si nanosheet.

The UV–Vis absorption spectra of the PANI–Si sheet composites differ significantly from those of the colloidal Si sheets. Fig. 6 shows UV-vis absorption spectra of bare PANI and the nanocomposites. The absorption spectra display five prominent bands centered at 256, 330, 418, 625 and 866 nm, respectively. The band observed at 256 nm corresponds to the characteristic benzenoid segment of PANI [41], while the peak

at 625 nm is associated with the quinoid structure [42]. The absorption at 328 nm arises from π–π* electronic transitions along the PANI backbone, representing the polymer in its reduced form. In contrast, the bands at 418 and 865 nm are indicative of the oxidized states of doped PANI [42], corresponding to two distinct polaron transitions: 418 nm for polaron-to-π* and 865 nm for π-to-polaron transitions [43]. The appearance of these three peaks at 328, 418, and 865 nm confirms the formation of the emeraldine salt of PANI. Furthermore, the UV–Vis analysis of both PANI and its composites demonstrates the coexistence of mixed oxidation states, a key requirement for electrical conductivity. The observation of polaron bands also suggests the presence of polaron quasi-particles, which are expected to play a significant role in charge transport.

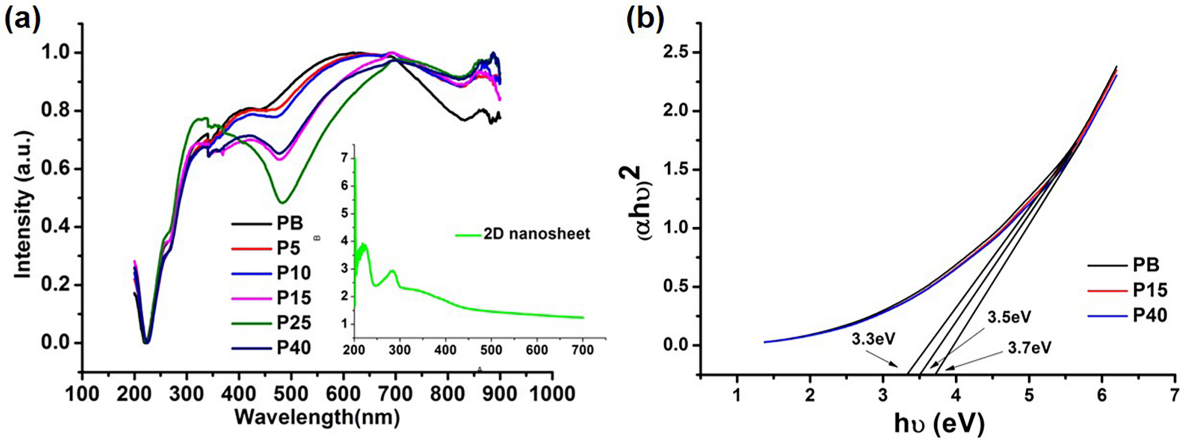

Figure 6: (**a**) UV-vis spectra of different composite samples. (**b**) Tauc's plot for pure PANI and PANI-Si sheet composites (only P15 and P40 are shown).

Upon Si addition, with an increase in the Si percentage, a red shift of the 625 nm peak confirms the interaction between PANI's quinoid rings and the Si sheets. We have detected a direct bandgap of our quasi 2D Si sample at 3.5 eV. We also detected a broad hump in the absorption profile that extends from 300–500 nm in the visible region and suggests the availability of states in this region. Electron density from π orbitals of PANI is transferred to these available energy states or vacant d orbital of Si which results in the red shift of these peaks. With an increase in Si content, the intensity of the peak at 865 nm becomes stronger. This behavior can be attributed to the interaction between the quinoid rings of PANI in its emeraldine salt form and the Si sheets, which promotes charge transfer via the reactive imine groups. Previous studies have indicated that strong interactions in organic–inorganic composites often arise from hydrogen bonding, leading to reduced orbital overlap and consequently enhanced intensity in the doped state [44]. Overall, the absorption characteristics are predominantly governed by PANI. From Tauc's plot (Fig. 6b), the band gap of pristine PANI is determined to be 3.3 eV, while the band gaps of the composites show a slight increase.

PL spectra of a fixed volume of the prepared Si sheet and the composites were carried out at room temperature. The PL spectra of Si nanosheet under different excitation energies are shown in Fig. 7a. The normalized spectra make it clear that the PL profile and peak positions remain the same, irrespective of the excitation energy. Such an observation suggests that the PL is intrinsic to the Si nanostructures and unlikely to be associated sensitively with size as that would have affected an excitation dependence for a distributed sample. We are inclined to believe that the observed PL is primarily dictated by the numerous surface/interface states, that appear inside the widened quantum confined band gap of nano Si.

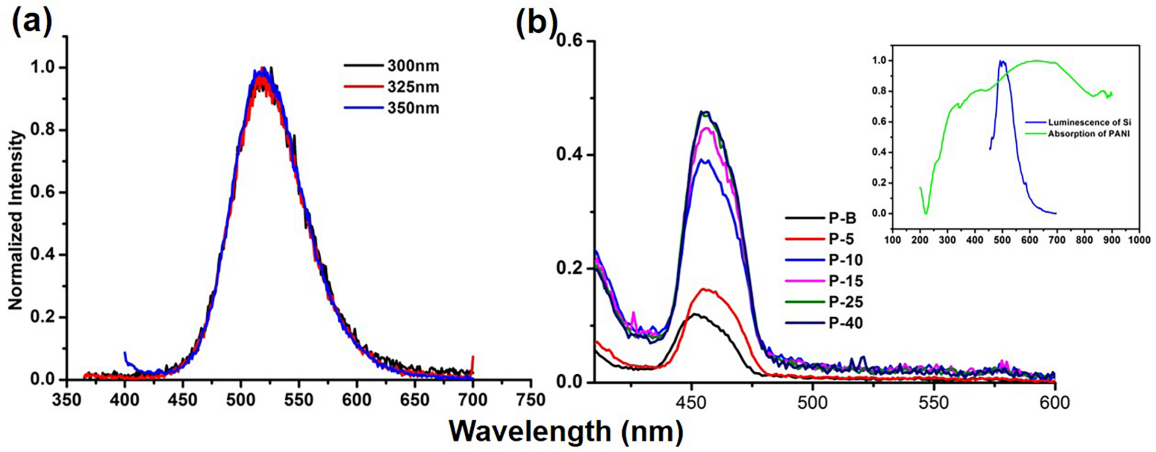

Figure 7: (**a**) PL Spectra of Si nanosheet under different excitation energies. (**b**) Composite samples along with blank PANI, combined PL of Si sheet and absorbance of PANI (inset).

Under 325 nm excitation, the PL spectrum shows an almost Gaussian peak at 540 nm. Despite decades of research on light-emitting Si nanostructures, the exact mechanism of emission has yet to be fully established [45–47]. Bulk Si being an indirect band gap material is an inefficient light emitter. But, when Si crystals are reduced to the nanoscale dimensions, they emit visible light. Surface states, oxides and suboxides, presence of chromophores, and most importantly a combined contribution of quantum confinement, surface and oxide effects were proposed to be responsible behind the observed luminescence [39].

The PL spectra of aqueous PANI under 325 nm excitation are shown in Fig. 7b, revealing very weak emission. This photoluminescence originates from the delocalized π-conjugated electrons and $\pi^*-\pi$ transitions of the benzenoid segments of polyaniline. It has been reported that, the benzenoid form of PANI shows luminescence, but, when it is oxidized in its quinoid form, no luminescence is observed [48], luminescence of blank PANI is more or less quenched due to the presence of quinoid.

PL spectrum of the composites are shown in Fig. 7b and the co-plot of PL of Si sheets and absorbance of PANI is shown as an inset, Fig. 7b. PL intensity of the PANI composite increases with increasing concentrations of Si nanosheets. The PL QY of the Si sheet was estimated to be ~9% whereas the PLQY of the P-40 sample is ~11%. When Si sheet is incorporated into PANI, a luminescent peak is observed with an excitation of 325 nm. PANI serves as a good electron donor and hole transporter, whereas quasi-2D silicon is an electron-conducting semiconductor with a band gap near 3.5 eV. The overlap between Si emission and PANI absorption is shown as the inset of Fig. 7b. In PANI, there are electron-donating groups like =NH and Si can accept electrons, which results in improved electron mobility in the system [49]. The incorporation of Si, with its distinct band gap, introduces numerous energy levels that facilitate photon-induced transitions between bonding and antibonding orbitals, leading to electron–hole recombination. Therefore, interfacial charge transfer occurs and there may be a chance of the formation of singlet exciton states in the composite system. These states decay radiatively to the ground state resulting in the observed enhanced PL in the system [50,51].

Previous studies have demonstrated that PANI–2D material composites significantly enhance electrical, optical, and electrochemical properties due to strong interfacial interactions and synergistic effects between the components [52–54]. Studies on PANI-based composites have demonstrated that the inclusion of carbon nanostructures significantly influences electrical and optical properties. For example, polyaniline composites with carbon nanotubes (PANI/CNT) have been reported to exhibit electrical conductivity values that are

markedly higher than pristine PANI due to the formation of conducting networks; in one study the electrical conductivity of crosslinked CNT/PANI composites reached up to ~12 S/cm at appropriate CNT loadings, significantly higher than typical PANI alone and attributed to effective charge transport pathways introduced by the CNT component [55].

Similarly, composites of PANI with graphene quantum dots (GQDs) and carbon quantum dots (CQDs) have been investigated for their optical and electronic properties. In CQDs/PANI composites designed for sensing applications, the quantum dots exhibited a fluorescence quantum yield of ~17% and significant quenching effects upon composite formation, indicating strong interaction between the dot and polymer components [56]. Limited reports also exist on GQD/PANI hybrids, where TEM and UV–vis analyses indicate effective interaction and changes in optical transitions due to charge transfer between GQDs and PANI chains, although detailed photoluminescence quantum yield data are often not the focus of these studies [43].

In contrast to these materials, our silicon-PANI composites are positioned as an exploratory class of 2D-silicon-based hybrid systems, with fundamental optical and structural characterization. While direct numerical comparisons of electrical conductivity or photoluminescence quantum yield with every type of PANI hybrid are limited by differences in measurement conditions and material form factors across studies, the existing literature establishes that:

- PANI/CNT composites typically show enhanced electrical conductivity relative to pure PANI due to CNT bridging effects and percolation networks [55].
- PANI/CQD or PANI/GQD composites exhibit optoelectronic interactions (such as fluorescence quenching and altered absorption features) arising from strong coupling between quantum dots and polymer chains, which can also influence photoluminescence behaviour [56].

Table 1 represents the values of electrical conductivity and photoluminescence quantum yield of the existing literatures compared with this work.

Table 1: Values of Electrical conductivity and photoluminescence Quantum yield of PANI based composites compared with the results of this work.

Composite System	Nanofiller Type	Key Reported Properties	Typical Values/Observations	Representative References
PANI (pristine)	—	Electrical conductivity	~10^{-3}–10^{-1} S cm^{-1} (doping dependent)	Stejskal, *Pure Appl. Chem.*, 2002 [57]
PANI/CNT	1D carbon nanotubes	Electrical conductivity enhancement via percolation networks	Up to ~10–12 S cm^{-1} at optimal CNT loading	Zhang, *Nanomaterials*, 2015 [58]
PANI/Graphene	2D graphene sheets	Improved conductivity and charge transport	~1–10 S cm^{-1} (varies with graphene content)	Stankovich et al., *Nature*, 2006 [59]

(Continued)

Table 1 (continued)

Composite System	Nanofiller Type	Key Reported Properties	Typical Values/Observations	Representative References
PANI/CQD	Carbon quantum dots (0D)	Strong PL interaction, fluorescence quenching	CQD QY ~10%–20%; PL quenching after composite formation	Wang et al., *Sens. Actuators B*, 2021 [60]
PANI/Si nanosheets (this work)	**Quasi-2D silicon nanosheets**	Structural integrity, tunable optical absorption, PL modulation	Systematic PL and absolute QY reported; dispersion confirmed by TEM	**This work**

4 Conclusion

In summary, we successfully prepared quasi 2D Si sheets by exfoliation of layered silicide and successfully combined them with a conducting polymer, PANI, to form nanocomposites containing different percentages of Si nanosheets. Structural investigations revealed the formation of a network of quasi 2D Si in a PANI matrix that itself consisted of a mixture of rods and sheets. Formation of the conducting emeraldine salt form of PANI and its presence in the nanocomposite samples were confirmed by spectroscopic investigations. Importantly, the Si nanosheets, as well as all the nanocomposite samples, were found to exhibit bright room temperature PL. We noted that the addition of Si nanosheets to PANI improved the PL QY. The properties of this nanocomposite material can be tuned easily by varying the concentration of quasi 2D Si, which in turn opens up scope for further research on this remarkable material.

Acknowledgement: Debosmita Karar acknowledges Dr. Mitun Das, Senior Principal Scientist and Divisional Chair, Biomaterials and Medical Devices Division, CGCRI, Kolkata.

Funding Statement: This research was funded by IIEST, Shibpur PhD fellowship.

Author Contributions: The authors confirm contribution to the paper as follows: Conceptualization, Debosmita Karar and Mallar Ray; methodology, Debosmita Karar and Mallar Ray; formal analysis, Debosmita Karar; investigation, Debosmita Karar; TEM investigation, Ashit Kumar Pramanick; writing—review and editing, Debosmita Karar. All authors reviewed and approved the final version of the manuscript.

Availability of Data and Materials: All data supporting the results of this study are included within the article.

Ethics Approval: Not applicable.

Conflicts of Interest: The authors declare no conflicts of interest.

References

1. Takeda K, Shiraishi K. Theoretical possibility of stage corrugation in Si and Ge analogs of graphite. Phys Rev B. 1994;50(20):14916–22. doi:10.1103/physrevb.50.14916.
2. Kopciuszynski M, Stępniak-Dybala A, Zdyb R, Krawiec M. Emergent Dirac fermions in epitaxial planar silicene heterostructure. Nano Lett. 2024;24(7):2175–80. doi:10.1021/acs.nanolett.3c04046.

3. Li WZ, He Y, Mao Y, Xiong K. Electronic properties and electrocatalytic water splitting activity for precious-metal-adsorbed silicene with nonmetal doping. ACS Omega. 2022;7(37):33156–66. doi:10.1021/acsomega.2c03388.
4. Khan K, Tareen AK, Aslam M, Wang R, Zhang Y, Mahmood A, et al. Recent developments in emerging two-dimensional materials and their applications. J Mater Chem C. 2020;8(2):387–440.
5. Shanmugam V, Mensah RA, Babu K, Gawusu S, Chanda A, Tu Y, et al. A review of the synthesis, properties, and applications of 2D materials. Mater Today Chem. 2022;39(6):2200031. doi:10.1002/ppsc.202200031.
6. Shan G, Tan H, Ma R, Zhao H, Huang W. Recent progress in emergent two-dimensional silicene. Nanoscale. 2023;15(7):2982–96. doi:10.1039/d2nr05809j.
7. Dávila ME, Le Lay G. Silicene: genesis, remarkable discoveries, and legacy. Mater Today Adv. 2022;16(41):100312. doi:10.1016/j.mtadv.2022.100312.
8. Uddin MM, Kabir MH, Ali MA, Hossain MM, Khandaker MU, Mandal S, et al. Graphene-like emerging 2D materials: recent progress, challenges and future outlook. RSC Adv. 2023;13:33336–75.
9. Nakano H, Mitsuoka T, Harada M, Horibuchi K, Nozaki H, Takahashi N, et al. Soft synthesis of single-crystal silicon monolayer sheets. Angew Chem Int Ed. 2006;45(38):6303–6. doi:10.1002/anie.200600321.
10. Nakano H, Ishii M, Nakamura H. Preparation and structure of novel siloxene nanosheets. Chem Commun. 2005;(23):2945–7. doi:10.1039/b500758e.
11. Lalmi B, Oughaddou H, Enriquez H, Kara A, Vizzini S, Ealet B, et al. Epitaxial growth of a silicene sheet. Appl Phys Lett. 2010;97(22):223109. doi:10.1063/1.3524215.
12. Fleurence A, Friedlein R, Ozaki T, Kawai H, Wang Y, Yamada-Takamura Y. Experimental evidence for epitaxial silicene on diboride thin films. Phys Rev Lett. 2012;108(24):245501. doi:10.1103/physrevlett.108.245501.
13. Lin CL, Arafune R, Kawahara K, Kanno M, Tsukahara N, Minamitani E, et al. Substrate-induced symmetry breaking in silicene. Phys Rev Lett. 2013;110(7):076801. doi:10.1103/physrevlett.110.076801.
14. Cahangirov S, Audiffred M, Tang P, Iacomino A, Duan W, Merino G, et al. Electronic structure of silicene on Ag(111): strong hybridization effects. Phys Rev B. 2013;88(3):035432. doi:10.1103/physrevb.88.035432.
15. Karar D, Bandyopadhyay NR, Pramanick AK, Acharyya D, Conibeer G, Banerjee N, et al. Quasi-two-dimensional luminescent silicon nanosheets. J Phys Chem C. 2018;122(33):18912–21. doi:10.1021/acs.jpcc.8b03988.
16. Go J, Kim J, Ju S, Yang D, Kang S, Park H. Hybrid interfaces of 2D materials with polymers for emerging electronics and energy devices. Materials. 2026;19(3):602. doi:10.3390/ma19030602.
17. Dresselhaus MS, Chen G, Tang MY, Yang RG, Lee H, Wang DZ, et al. New directions for low-dimensional thermoelectric materials. Adv Mater. 2007;19(8):1043–53. doi:10.1002/adma.200600527.
18. Song E, Liu P, Lv Y, Wang E, Guo CY. Conductive polymer-based thermoelectric composites: preparation, properties, and applications. J Compos Sci. 2024;8(8):308. doi:10.3390/jcs8080308.
19. Epstein AJ, Ginder JM, Zuo F, Woo HS, Tanner DB, Richter AF, et al. Insulator-to-metal transition in polyaniline: effect of protonation in emeraldine. Synth Met. 1987;21(1–3):63–70. doi:10.1016/0379-6779(87)90067-1.
20. Gao XZ, Liu HJ, Cheng F, Chen Y. Thermoresponsive polyaniline nanoparticles: preparation, characterization, and their potential application in waterborne anticorrosion coatings. Chem Eng J. 2016;283:682–91. doi:10.1016/j.cej.2015.08.015.
21. Gilhotra C, Chander M, Sanjay. A review: conducting polyaniline polymer. AIP Conf Proc. 2019;2142:150008. doi:10.1063/1.5122557.
22. Beygisangchin M, Baghdadi AH, Kamarudin SK, Rashid SA, Jakmunee J, Shaari N. Recent progress in polyaniline and its composites: synthesis, properties, and applications. Eur Polym J. 2024;210(1998):112948. doi:10.1016/j.eurpolymj.2024.112948.
23. Bhat SV, Vivekchand SRC. Optical spectroscopic studies of composites of conducting PANI with CdSe and ZnO nanocrystals. Chem Phys Lett. 2006;433(1–3):154–8. doi:10.1016/j.cplett.2006.11.045.
24. Zhang S, Chen Q, Jing D, Wang Y, Guo L. Visible photoactivity and antiphotocorrosion performance of PdS-CdS photocatalysts modified by polyaniline. Int J Hydrogen Energy. 2012;37(1):791–6. doi:10.1016/j.ijhydene.2011.04.060.

25. Park OK, Jeevananda T, Kim NH, Kim SI, Lee JH. Effects of surface modification on the dispersion and electrical conductivity of carbon nanotube/polyaniline composites. Scr Mater. 2009;60(7):551–4. doi:10.1016/j.scriptamat.2008.12.005.
26. Huang F, Vanhaecke E, Chen D. *In situ* polymerization and characterizations of polyaniline on MWCNT powders and aligned MWCNT films. Catal Today. 2010;150(1–2):71–6. doi:10.1016/j.cattod.2009.05.017.
27. Lin YC, Hsu FH, Wu TM. Enhanced conductivity and thermal stability of conductive polyaniline/graphene composite synthesized by *in situ* chemical oxidation polymerization with sodium dodecyl sulfate. Synth Met. 2013;184:29–34. doi:10.1016/j.synthmet.2013.10.001.
28. Zhang Q, Li Y, Feng Y, Feng W. Electropolymerization of graphene oxide/polyaniline composite for high-performance supercapacitor. Electrochim Acta. 2013;90:95–100. doi:10.1016/j.electacta.2012.11.035.
29. Siddique AB, Morrison K, Venkat G, Pramanick AK, Banerjee N, Ray M. Charge transport through functionalized graphene quantum dots embedded in a polyaniline matrix. ACS Appl Electron Mater. 2021;3(3):1437–46. doi:10.1021/acsaelm.1c00057.
30. Pouget JP, Jozefowicz ME, Epstein AJ, Tang X, MacDiarmid AG. X-ray structure of polyaniline. Macromolecules. 1991;24(3):779–89. doi:10.1021/ma00003a022.
31. Chaudhari HK, Kelkar DS. Investigation of structure and electrical conductivity in doped polyaniline. Polym Int. 1997;42(4):380–4. doi:10.1002/(SICI)1097-0126(199704)42:4<380::AID-PI727>3.0.CO;2-F.
32. Yelil Arasia A, Jeyakumari J, Sundaresan B, Dhanalakshmi V, Anbarasan R. Structural properties of poly (aniline) via FTIR spectroscopy. Spectrochim Acta A. 2009;74:1229–34.
33. Cai JJ, Zuo PJ, Cheng XQ, Xu YH, Yin GP. Nano-silicon/polyaniline composite for lithium storage. Electrochem Commun. 2010;12(11):1572–5. doi:10.1016/j.elecom.2010.08.036.
34. Trchová M, Šeděnková I, Tobolková E, Stejskal J. FTIR spectroscopic and conductivity study of the thermal degradation of polyaniline films. Polym Degrad Stab. 2004;86(1):179–85. doi:10.1016/j.polymdegradstab.2004.04.011.
35. Grill A, Neumayer DA. Structure of low dielectric constant SiCOH films: FTIR characterization. J Appl Phys. 2003;94:6697–707.
36. Cotirlan-Simioniuc C, Ghita RV, Negrila CC, Logofatu C. The evanescent-wave cavity ring-down spectroscopy technique applied to the investigation of thermally grown oxides on Si(100). Appl Phys A. 2014;117(3):1359–65. doi:10.1007/s00339-014-8556-3.
37. Shanks H, Fang CJ, Ley L, Cardona M, Demond FJ, Kalbitzer S. Infrared spectrum and structure of hydrogenated amorphous silicon. Phys Status Solidi B. 1980;100(1):43–56. doi:10.1002/pssb.2221000103.
38. Fuchs HD, Stutzmann M, Brandt MS, Rosenbauer M, Weber J, Cardona M. Visible luminescence from porous silicon and siloxene. Phys Scr. 1992;T45:309–13. doi:10.1088/0031-8949/1992/t45/067.
39. Canham LT. Silicon quantum wire array fabrication by electrochemical and chemical dissolution of wafers. Appl Phys Lett. 1990;57(10):1046–8. doi:10.1063/1.103561.
40. Montalti M, Cantelli A, Battistelli G. Nanodiamonds and silicon quantum dots for bioimaging. Chem Soc Rev. 2015;44:4853–921.
41. Scotto J, Florit MI, Posadas D. About the species formed during the electrochemical half oxidation of polyaniline: polaron-bipolaron equilibrium. Electrochim Acta. 2018;268:187–94. doi:10.1016/j.electacta.2018.02.066.
42. Yang C, Fang Z, Zhang P. UV-Vis spectra of polyaniline doped with camphor sulfonic acid in different organic solvents. J Cent South Univ Technol. 1999;6(2):127–9. doi:10.1007/s11771-999-0014-6.
43. Maity N, Kuila A, Das S, Mandal D, Shit A, Nandi AK. Optoelectronic and photovoltaic properties of graphene quantum dot–polyaniline nanostructures. J Mater Chem A. 2015;3(41):20736–48. doi:10.1039/c5ta06576c.
44. Kannusamy P, Sivalingam T. Chitosan-ZnO/polyaniline hybrid composites. Polym Degrad Stab. 2013;98:988–96.
45. Luo JW, Li SS, Sychugov I, Pevere F, Linnros J, Zunger A. Absence of redshift in the direct bandgap of silicon nanocrystals with reduced size. Nature Nanotech. 2017;12(10):930–2. doi:10.1038/nnano.2017.190.
46. Abdelhameed M, Martir DR, Chen S, Xu WZ, Oyeneye OO, Chakrabarti S, et al. Tuning optical properties of silicon quantum dots. Sci Rep. 2018;8:3050.

47. Fu S, Zhang J, Li X, Jin E, Gao L, Dong R, et al. Fundamentals of charge transport in two-dimensional framework materials. Nat Rev Mater. 2025. doi:10.1038/s41578-025-00840-z.
48. Kim K, Lin LB, Ginder JM, Gustafson TL, Epstein AJ. Luminescence and picosecond photoinduced absorption of polyaniline. Synth Met. 1992;50(1–3):423–8. doi:10.1016/0379-6779(92)90195-o.
49. McCall RP, Ginder JM, Leng JM, Ye HJ, Manohar SK, Masters JG, et al. Spectroscopy and defect states in polyaniline. Phys Rev B. 1990;41(8):5202–13. doi:10.1103/physrevb.41.5202.
50. Bera S, Singh M, Thantirige R, Tiwary SK, Shook BT, Nieves E, et al. 2D-nanofiller-based polymer nanocomposites for capacitive energy storage applications. Small Sci. 2023;3(7):2300016. doi:10.1002/smsc.202300016.
51. Hasnan NSN, Nordin NA, Mohamed MA. Synergistic interaction of conducting polymer photocatalysts. J Mater Chem A. 2024;12:27892–910.
52. AhadiParsa M, Dehghani A, Ramezanzadeh B. Titanium carbide-based (Ti_3C_2) MXene@Zn-doped-S-polyaniline nanosheets: toward thermo-mechanical and UV-shielding properties enhancement. J Taiwan Inst Chem Eng. 2024;156:105364.
53. Muthuraman A, Pandiyan A, Veeramuthu L, Babu S, Jawaharlal H, Lin SY, et al. Structurally reinforced silk fibroin/MXene flexible biocomposite films for robust underwater self-powered electronic systems. ACS Appl Bio Mater. 2026;9(1):466–78. doi:10.1021/acsabm.5c02148.
54. Aldulaimi A, Saeed SM, Menon SV, Saber RY, Ray S, Jayabalan K, et al. Exploring recent advances and synthesis strategies in conductive polymers and their composites in supercapacitor systems: a comprehensive review. RSC Adv. 2025;15(53):45245–67. doi:10.1039/d5ra06603d.
55. Liu D, Wang X, Deng J, Zhou C, Guo J, Liu P. Crosslinked CNT/polyaniline composites as pseudocapacitive material. Nanomaterials. 2015;5:1034–47.
56. Ahmed HM, Ghali M, Zahra W, Ayad MM. Preparation of carbon quantum dots/polyaniline nanocomposite: towards highly sensitive detection of picric acid. Spectrochim Acta Part A Mol Biomol Spectrosc. 2021;260(3/4):119967. doi:10.1016/j.saa.2021.119967.
57. Stejskal J. Polyaniline: preparation of a conducting polymer. Pure Appl Chem. 2002;74:857–67.
58. Zhang H. Ultrathin two-dimensional nanomaterials. ACS Nano. 2015;9(10):9451–69. doi:10.1021/acsnano.5b05040.
59. Stankovich S, Dikin DA, Dommett GHB, Kohlhaas KM, Zimney EJ, Stach EA, et al. Graphene-based composite materials. Nature. 2006;442(7100):282–6. doi:10.1038/nature04969.
60. Wang N, Tao W, Gong X, Zhao L, Wang T, Zhao L, et al. Highly sensitive and selective NO_2 gas sensor fabricated from Cu_2O-CuO microflowers. Sens Actuat B Chem. 2022;362:131803. doi:10.1016/j.snb.2022.131803.